
This is an electronic reprint of the original article.
This reprint may differ from the original in pagination and typographic detail.

Ramaprakash, A. N.; Rajarshi, C. V.; Das, H. K.; Khodade, P.; Modi, D.; Panopoulou, G.; Maharana, S.; Blinov, D.; Angelakis, E.; Casadio, C.; Fuhrmann, L.; Hovatta, T.; Kiehlmann, S.; King, O. G.; Kylafis, N.; Kougentakis, A.; Kus, A.; Mahabal, A.; Marecki, A.; Myserlis, I.; Paterakis, G.; Paleologou, E.; Liodakis, I.; Papadakis, I.; Papamastorakis, I.; Pavlidou, V.; Pazderski, E.; Pearson, T. J.; Readhead, A. C.S.; Reig, P.; Słowikowska, A.; Tassis, K.; Zensus, J. A.

RoboPol

Published in:
Monthly Notices of the Royal Astronomical Society

DOI:
[10.1093/mnras/stz557](https://doi.org/10.1093/mnras/stz557)

Published: 01/05/2019

Document Version
Publisher's PDF, also known as Version of record

Please cite the original version:
Ramaprakash, A. N., Rajarshi, C. V., Das, H. K., Khodade, P., Modi, D., Panopoulou, G., Maharana, S., Blinov, D., Angelakis, E., Casadio, C., Fuhrmann, L., Hovatta, T., Kiehlmann, S., King, O. G., Kylafis, N., Kougentakis, A., Kus, A., Mahabal, A., Marecki, A., ... Zensus, J. A. (2019). RoboPol: A four-channel optical imaging polarimeter. *Monthly Notices of the Royal Astronomical Society*, 485(2), 2355-2366.
<https://doi.org/10.1093/mnras/stz557>

This material is protected by copyright and other intellectual property rights, and duplication or sale of all or part of any of the repository collections is not permitted, except that material may be duplicated by you for your research use or educational purposes in electronic or print form. You must obtain permission for any other use. Electronic or print copies may not be offered, whether for sale or otherwise to anyone who is not an authorised user.

RoboPol: a four-channel optical imaging polarimeter

A. N. Ramaprakash,¹★ C. V. Rajarshi,¹ H. K. Das,¹ P. Khodade,¹ D. Modi,¹
 G. Panopoulou,²★ S. Maharana,¹ D. Blinov,^{3,4,5} E. Angelakis,⁶ C. Casadio,⁶
 L. Fuhrmann,⁶ T. Hovatta,^{7,8} S. Kiehlmann,² O. G. King,² N. Kylafis,^{3,4}
 A. Kougentakis,³ A. Kus,⁹ A. Mahabal,² A. Marecki,⁹ I. Myserlis,⁶ G. Paterakis,³
 E. Paleologou,³ I. Liodakis,¹⁰ I. Papadakis,^{3,4} I. Papamastorakis,^{3,4} V. Pavlidou,^{3,4}
 E. Pazderski,⁹ T. J. Pearson,² A. C. S. Readhead,² P. Reig,^{3,4} A. Słowikowska,⁹
 K. Tassis,^{3,4} and J. A. Zensus⁶

¹Inter-University Centre for Astronomy & Astrophysics, Post bag 4, Ganeshkhind, Pune 411007, India

²Cahill Center for Astronomy and Astrophysics, California Institute of Technology, 1200 E California Blvd, MC 249-17, Pasadena, CA 91125, USA

³Foundation for Research and Technology – Hellas, IA & IESL, Voutes, 71110 Heraklion, Greece

⁴Department of Physics and Institute of Theoretical & Computational Physics, University of Crete, PO Box 2208, GR-710 03, Heraklion, Crete, Greece

⁵Astronomical Institute, St. Petersburg State University, Universitetsky pr. 28, Petrodvoretz, 198504 St. Petersburg, Russia

⁶Max-Planck-Institut für Radioastronomie, Auf dem Hügel 69, 53121 Bonn, Germany

⁷Finnish Centre for Astronomy with ESO (FINCA), University of Turku, FI-20014, Turku, Finland

⁸Aalto University Metsähovi Radio Observatory, Metsähovintie 114, 02540 Kylmälä, Finland

⁹Toruń Centre for Astronomy, Nicolaus Copernicus University, Faculty of Physics, Astronomy and Informatics, Grudziadzka 5, 87-100 Toruń, Poland

¹⁰KIPAC, Stanford University, 452 Lomita Mall, Stanford, CA 94305, USA

Accepted 2019 February 21. Received 2019 February 20; in original form 2019 January 8

ABSTRACT

We present the design and performance of RoboPol, a four-channel optical polarimeter operating at the Skinakas Observatory in Crete, Greece. RoboPol is capable of measuring both relative linear Stokes parameters q and u (and the total intensity I) in one sky exposure. Though primarily used to measure the polarization of point sources in the R band, the instrument features additional filters (B , V , and I), enabling multiwavelength imaging polarimetry over a large field of view ($13.6' \times 13.6'$). We demonstrate the accuracy and stability of the instrument throughout its 5 yr of operation. Best performance is achieved within the central region of the field of view and in the R band. For such measurements the systematic uncertainty is below 0.1 per cent in fractional linear polarization, p (0.05 per cent maximum likelihood). Throughout all observing seasons the instrumental polarization varies within 0.1 per cent in p and within $\sim 1^\circ$ in polarization angle.

Key words: instrumentation: polarimeters – techniques: polarimetric.

1 INTRODUCTION

Modern polarimeter design is driven by diverse science goals. Examples include the aim to detect the extremely low polarization signature of planets near bright stars (Hough et al. 2006; Wiktorowicz & Nofi 2015), or the wavelength dependence of time-varying polarization through synchronous multiband imaging (Piirola, Berdyugin & Berdyugina 2014).

The most commonly used design for imaging polarimetric instruments is the dual-beam polarimeter (e.g. Appenzeller 1967), which

at its heart combines a modulator/retarder (e.g. rotating half-wave plate) with a beam analyser (e.g. birefringent prism). Compared to its predecessor, the single-beam polarimeter, this type of instrument offers the advantage of cancellation of multiplicative noises that affect the two beams (such as variations in atmospheric opacity between exposures) (Scarrott et al. 1983). This design allows only for measurement of one polarized Stokes parameter (Q or U for linear polarimetry) at a time. In order to obtain the fractional linear polarization, p , and polarization position angle, χ , (and also to break the mirror degeneracy of the latter), at least two exposures at different orientations of the half-wave plate (usually at 0° and 22.5°) are necessary. In practice, to correct for instrumental effects such as differential response of the polarimeter to different polarization

* E-mail: anr@iucaa.in (ANR); panopg@caltech.edu (GP)

states of incoming light, two additional exposures are taken at 45° and 67.5° (e.g. Magalhaes et al. 1996; Ramaprakash et al. 1998). So a typical polarization measurement with a dual-beam polarimeter consists of four exposures at different half-wave plate positions. Dual-beam polarimetry is susceptible to target variations between exposures, incorrect alignment of the half-wave plate, and can have large CCD readout time overheads.

These constraints are bypassed in the quadruple-beam (or four-channel) polarimeter design. First proposed by Geyer et al. (1996), the four-channel polarimeter uses a pair of birefringent prisms (in this case Wollaston prisms, WPs) as the beam analyzer to achieve simultaneous measurement of both Stokes Q and U . Four beams polarized at 0° , 45° , 90° , and 135° emerge out of this prism pair. The measurement of the relative intensities of the first two beams provides the Stokes parameter Q (0° , 90°) and relative intensities of the other two beams provides U . The prisms are placed in such a way that the telescope beam is shared approximately equally between the two, and all polarization states are imaged simultaneously at different positions on the detector. This basic principle has been implemented in a number of existing instruments (e.g. Pernechele, Giro & Fantinel 2003; Fujita, Itoh & Mukai 2009; Helhel et al. 2015; Devogèle et al. 2017).

The efficiency of a four-channel instrument at first glance seems inferior to that of the dual-channel design: the light of the source is split into four rays, compared to two in the dual-beam design. However, in reality the four-channel design does not lead to any loss of performance, due to the fact that the uncertainty on a Stokes parameter measurement depends on the noise of the total intensity (the sum of the two beams) used to obtain the Stokes parameter, and not that of a single beam. Thus, a four-channel instrument can achieve the same accuracy, in terms of photon noise, as a (perfect) dual-beam instrument in only twice the time. However, the control of systematics in dual-beam polarimetry, which requires a minimum of four exposures, results in the same amount of exposure time as in the four-channel case. With the four-channel set-up, any inaccuracies due to the positioning of a rotating retarder, or other systematics due to instrument changes between exposures, are avoided at no cost in terms of timing.

RoboPol is a four-channel polarimeter, capable of measuring the linear Stokes parameters in one exposure. A collimated telescope beam is shared equally by two quartz WPs, each with its own half-wave plate in front. Four beams of differing polarization states are output from this system, and are imaged on a CCD detector. Relative photometry of the four beam images provides the linear Stokes parameters. RoboPol is mounted on the 1.3 m telescope of the Skinakas observatory in Crete, Greece. The instrument was custom designed and built to conduct a comprehensive long-term blazar polarimetric monitoring campaign.

Operating successfully since 2013, data collected by RoboPol have contributed in multiple publications in the field of blazars (Pavlidou et al. 2014; Blinov et al. 2015, 2016a,b; Angelakis et al. 2016; Hovatta et al. 2016; Kiehlmann et al. 2017; Liodakis et al. 2017; Raiteri et al. 2017; Uemura et al. 2017; Blinov et al. 2018), galactic binaries and white dwarfs (Reig et al. 2014; errorZdotejmo et al. 2017; Reig, Blay & Blinov 2017; Reig & Blinov 2018; Słowikowska et al. 2018), gamma-ray bursts (King et al. 2014b), and the interstellar medium (Panopoulou et al. 2015; Panopoulou, Psaradaki & Tassis 2016; Skalidis et al. 2018).

We present the instrumental design in Section 2. Section 3 describes the commissioning phase. We demonstrate the accuracy and long-term stability of the instrument in Section 4. We summarize in Section 5.

2 THE INSTRUMENT

2.1 Design considerations

The main scientific driver for building RoboPol was to explore the nature of the coherent rotation of the polarization angle of blazar optical emission, first observed three decades ago (e.g. Kikuchi et al. 1988). Although different mechanisms have been proposed to explain this behaviour (e.g. Björnsson 1982; Konigl & Choudhuri 1985; Sillanpää et al. 1993; Abdo et al. 2010), observational evidence has lagged behind. This was our main motivation for initiating the RoboPol blazar monitoring campaign. The project goal was to observe the linear optical polarization of a large, statistically unbiased sample of blazars with high cadence for a duration of 3 yr (Pavlidou et al. 2014).

The RoboPol polarimeter has been developed with two main priorities in mind: efficiency and accuracy. The large sample of targets (~ 100) to be covered with a cadence of several days calls for high observing efficiency (with minimal overheads such as pointing and slewing). The optical emission from blazars is typically linearly polarized at a level of a few per cent (Pavlidou et al. 2014). For the limiting case of a source with fractional linear polarization, p , of 1 per cent and $R = 18$ mag the instrument should be capable of producing a 3σ detection within 30 min of exposure time. Systematic uncertainties should therefore be below $\sigma_p = 0.3$ per cent.

According to these considerations, a four-channel design was selected for RoboPol as it meets the needs of the scientific program: high measurement accuracy with minimal overheads. In order to minimize the amount of time spent on a specific target, monitoring is performed in a single band (Johnson–Cousins R).

The instrument is also capable of performing complementary science in the B , V , and I bands (through the use of a filter wheel). The instrument features a large field of view (FOV) (13.6×13.6 arcmin). This provides the benefit of performing relative photometry for the central target source (to obtain Stokes I). This also enables rapid polarimetric mapping of point sources over large areas on the sky.

2.2 Telescope and CCD camera

The polarimeter has been designed for (and is mounted on) the 1.3 m Ritchey–Chrétien telescope at the Skinakas observatory in Crete. The telescope¹ has the following specifications: 129 cm \odot primary $f/2.88$, 45 cm \odot secondary $f/4.39$, telescope $f/7.64$ and an equatorial mount. To satisfy the spatial needs of the instrument, the telescope’s focus was repositioned, by altering the distance between the primary and secondary mirrors by 15.281 mm. This resulted in a shift of the focus position of 120 mm towards the primary, setting the telescope to an f-number of $f/7.488$.

RoboPol is mounted on the direct port of the standard Guidance and Acquisition Module (GAM) at the Cassegrain focal station of the telescope. Along with RoboPol, the telescope is equipped with other instruments, including an imaging camera, an infrared camera, and a spectrograph. The telescope beam can be diverted to one of the side port instruments by a fold mirror on a linear stage. The mirror is stowed out of the way when RoboPol is in use. We avoided using the side port for RoboPol to eliminate instrument polarization that would be introduced by the science fold mirror.

¹<http://skinakas.physics.uoc.gr/en/>

The detector used for RoboPol, provided by the Skinakas Observatory, is an Andor DW436 CCD camera with 2048×2048 pixels of size $13.5 \mu\text{m}$. By the use of a Peltier device, the camera can be cooled to -70°C ensuring negligible dark current ($6 \times 10^{-4} e^-/\text{s}/\text{pix}$). The gain and the readout noise at the $2 \mu\text{s pix}^{-1}$ readout speed that we use are $2.687 e^-/\text{ADU}$ and $8.14 \pm 0.12 e^-$, respectively. The median seeing at Skinakas is 1 arcsec. At the camera the focal ratio of $f/5$ gives a mean pixel angular size of ~ 0.4 arcsec, and an FOV of 13.6 arcmin. The defocusing of the secondary leads to image quality degradation at the telescope focal plane. However, this is adequately accounted for and compensated by the instrument's optics so that the final delivered image quality on the CCD meets the design requirements.

2.3 Optical design

A side view of the optical design of RoboPol is shown in Fig. 1. The optical design of the instrument was optimized after including the defocused telescope optics. A combination of lenses collimates the beam from the telescope focal plane and transfers it to the polarization-analyzing system. For simplicity, we only show the rays output from one of the WPs. The output beams are imaged on the CCD detector by the camera assembly. The telescope and mount structure place stringent space constraints on the instrument design. As a result, the instrument is very compact, measuring only 421 mm in length.

The polarization optics of the system are shown schematically in Fig. 2. The telescope beam is shared by a pair of half-wave plates followed by a pair of WPs. The angle θ of the optical axis of the elements is measured clockwise from the y -axis as shown on the CCD plane in Fig. 2. The left half (as shown in Fig. 2) of the beam is transmitted through a half-wave plate with fast axis at $\theta = 0^\circ$. It subsequently passes through a WP with axis also at $\theta = 0^\circ$. A light ray transmitted through this pair of elements is split into two rays with orthogonal polarizations: an extraordinary ray (e-ray, with electric field at $\theta = 0^\circ$) and an ordinary ray (o-ray, with electric field at $\theta = 90^\circ$). The o- and e-rays diverge horizontally (along x). The right half of the beam is transmitted through a half-wave plate with optical axis at $\theta = 67.5^\circ$. The subsequent WP has its axis at $\theta = 90^\circ$ and splits light rays vertically. Thus, the polarization angle of the beam incident on the WP on the right-hand side is effectively rotated by 45° with respect to the prism axis. All elements of the system are fixed and do not move. The specifications of the polarization optics are listed in Table 1.

Fig. 3 shows $Zemax^2$ spot diagrams for modeled point sources placed at different locations within the FOV (different panels). Rays of three different wavelengths (all within the R band) were traced and are shown with different colours. For simplicity, we only show the predictions for one half of the pupil beam passing through a set of half-wave plate and WP.

The pattern of divergence of the rays from the origin depends strongly on location in the FOV but only slightly on the wavelength. Any chromaticity induced within the instrument (mainly the WP) is small compared to the size of the typical PSF. The least divergence is seen for a source placed at the center of the field (at $(0^\circ, 0^\circ)$ top left-hand panel), where the maximum divergence is $11 \mu\text{m}$. The highest divergence is $47 \mu\text{m}$, at $(0^\circ, 0.1125^\circ)$. The RMS radial divergence of the rays for a given location on the FOV ranges from $6 \mu\text{m}$ to $23.5 \mu\text{m}$.

This RMS radius can be taken as a rough estimate of the PSF size (without the effect of atmospheric seeing). We compare these values to the expected atmospheric seeing. A PSF of 1 arcsec (median seeing at the Skinakas Observatory) is fully sampled with 2.5 pixels (with 0.4 arcsec per pixel on average). This corresponds to a radius of $16.9 \mu\text{m}$, for a pixel size of $13.5 \mu\text{m}$. For the central source, therefore, the PSF is predicted to be seeing-limited. This is not the case for sources placed in the majority of locations on the FOV. In Section 3 we compare these predictions to the actual measured performance of the instrument in terms of encircled energy diagrams.

Differential photometry of the pair of vertical spots gives the relative Stokes parameter u , and that of horizontal spots gives q^3 :

$$q = \frac{N_2 - N_3}{N_2 + N_3}, \quad u = \frac{N_1 - N_0}{N_0 + N_1}, \quad (1)$$

where N_i is the photon count of the spot with index i (from 0 to 3) as shown in Fig. 2.⁴ The photon counts N_i result after correcting the measured counts for sky background. The uncertainties of the Stokes parameters are given by the following equations (by error propagation, see also Ramaprakash et al. 1998):

$$\sigma_q = \sqrt{\frac{4(N_2^2\sigma_3^2 + N_3^2\sigma_2^2)}{(N_3 + N_2)^4}}, \quad \sigma_u = \sqrt{\frac{4(N_0^2\sigma_1^2 + N_1^2\sigma_0^2)}{(N_0 + N_1)^4}}, \quad (2)$$

while the uncertainties of the intensities, σ_i , are calculated according to Laher et al. (2012):

$$\sigma_i = \sqrt{N_i + \sigma_{\text{sky}}^2 A_{\text{phot}} + \frac{\sigma_{\text{sky}}^2 A_{\text{phot}}^2}{A_{\text{sky}}}}, \quad (3)$$

where $\sigma_{\text{sky}}^2 = n_{\text{sky}}$ is the average sky intensity (background) in a single pixel, A_{phot} is the area (in pixels) of the photometry aperture, and A_{sky} is the area of the annulus used for background estimation. The first two terms account for the photon counting statistics of the source and sky, and the third describes the background estimation uncertainty.

The design of RoboPol⁵ differs from that of most four-channel polarimeters. It uses a half-wave plate to rotate one half of the incoming light instead of a modified WP such as that proposed by Geyer et al. (1996). In this respect it is similar to the design described in Fujita et al. (2009). However, Fujita et al. (2009) used a beam splitter to divert half of the beam to one of the prisms, and channeled that part of the beam on the detector by the use of a folding mirror. RoboPol's design, in contrast, avoids the large instrumental polarization induced by a folding mirror.

Another difference with other four-channel designs is that the WPs do not contain wedges such as those proposed by Oliva (1997) and implemented in many instruments (Percechele et al. 2003; Kawabata et al. 2008; Afanasiev & Amirkhanyan 2012; Covino et al. 2014; Helhel et al. 2015; Devogèle et al. 2017). As a result, there is significant vignetting throughout RoboPol's FOV (Fig. 4). Additionally, there are well-described geometric distortions that cause the four-spot pattern to vary as a function of position.

³The normalized Stokes parameters are defined as $q = Q/I$ and $u = U/I$, where I is the total intensity and Q and U are the linear polarization Stokes parameters.

⁴We note that our equations 1 differ from those given in King et al. (2014a) due to a typographical error in the latter.

⁵The authors are happy to share more design details through private communication.

²www.zemax.com

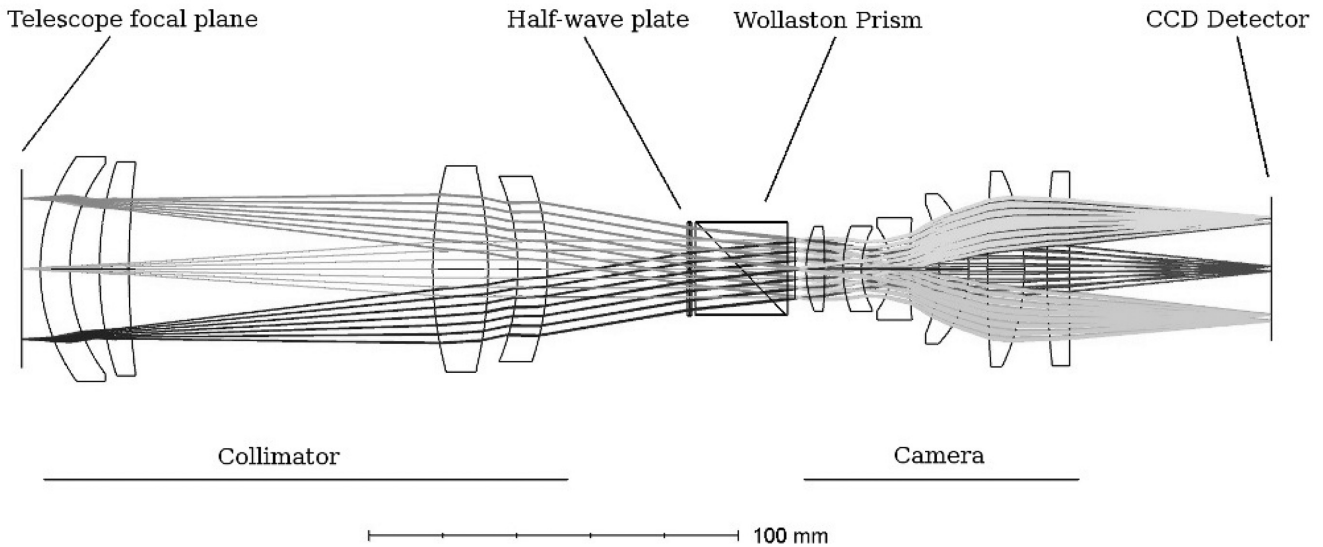


Figure 1. Optical design of RoboPol (side view). The optical train from left to right: telescope focal plane, collimator lenses, half-wave plates and WPs system, camera lenses, CCD. Light rays originating at different locations on the FOV are shown as they propagate through the system (differently shaded grey lines).

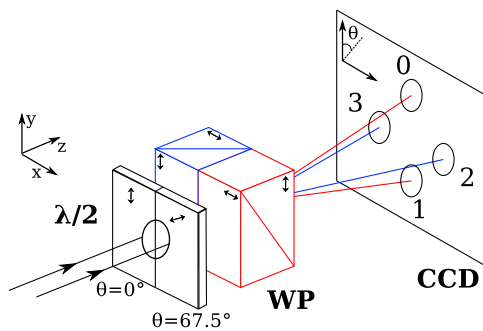


Figure 2. Schematic of the half-wave plate ($\lambda/2$) and WP system of RoboPol. The fast optical axes of the elements are shown with bidirectional arrows. The angle of the axis, θ , is denoted below each half-wave plate.

These effects are taken into account in the modeling of the instrumental response described in Section 3.

2.4 Mask

The four-channel design of RoboPol has two disadvantageous consequences due to the fact that any point on the CCD receives photons from four different regions of the sky: (a) the photon background (noise) is increased compared to (e.g.) dual-beam polarimetry and (b) neighbouring sources on the sky can overlap as projected on the CCD. To address these issues, it is customary in four-channel polarimetry to place a mask that blocks light from nearby regions of the observed target field, reducing the sky background (e.g. Kawabata et al. 2008). We followed this approach in order to increase the measurement accuracy, but only for the central target.

Fig. 5 (left-hand panel) shows the mask design and its supporting legs. The middle panel shows a schematic of the mask (center of the left-hand panel). Open (unblocked) regions are colored white, while the areas that are blocked by the mask are colored black. The light from the central square (marked ‘x’) is projected on the $\sim 21''$ -wide squares marked 0–3. Square 3 receives light from the central square

Table 1. WP and half-wave plate characteristics.

WPs	
Material	Quartz
Size	25 × 25 mm
Clear aperture	22.5 mm minimum
Divergence	60 arcmin in the visible
Wavelength range	400–900 nm
Extinction ratio	$< 10^{-4}$
Wavefront distortion	$< \lambda$ at 633nm
AR coating	$R < 0.7\%$ over 500–900 nm on both surfaces
Manufacturer	Karl Lambrecht corp.
Half-wave plates	
Material	MgF2 and Quartz crystal (cemented)
Retardation	$\lambda/2 \pm 5\%$ over 400–900 nm
Beam deviation	$< 1'$
Wavefront distortion	$< \lambda$ at 633nm
Accuracy of axis orientation	$\pm 30'$
Size	25 × 25 mm
AR coating	$R < 0.5\%$ over 500–900 nm on both surfaces
Manufacturer	Karl Lambrecht corp.

(‘x’) but not from squares a, b, and c. It receives one-quarter of the light reaching the central square. The remaining three-quarters of the light from the central square are divided among regions 1, 2, and 0. As a consequence, the background for the central source is reduced by a factor of ~ 4 compared to the majority of the FOV. The right-hand panel of Fig. 5 shows the shadows cast by the mask during a science exposure with RoboPol.

The support structure of the mask can be seen extending in four directions in Figs 4 and 5. Along with the mask, these supports cast shadows, reducing the available for polarimetry area to ~ 85 per cent of the total (13.6×13.6 arcmin) FOV. The mask appears unfocused as it is not located exactly at the focal plane. This was necessitated due to the need to contain the instrument within the space available.

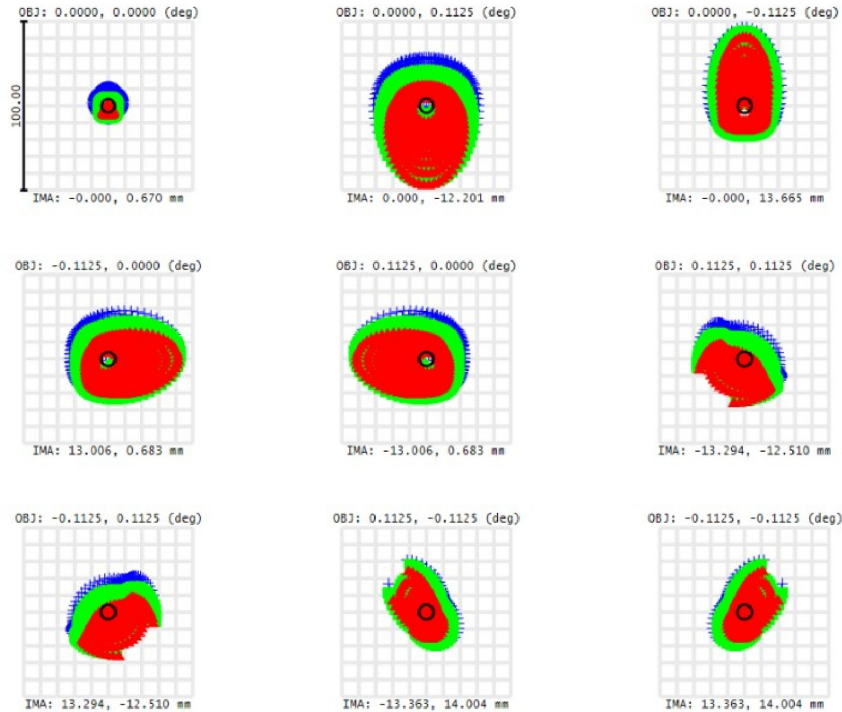


Figure 3. Instrument spot diagrams for one of the images formed by one of the RoboPol WP – half-wave plate pairs. The image was created using the Zemax software and does not take into account atmospheric seeing. Each panel shows the predicted image for a different position on the FOV. The positions are labeled above each panel. The top left-hand panel shows the image at the center of the FOV, at coordinates (0,0). Other panels show images near the edges of the FOV. Different colors show the image for different input wavelengths: 600 nm, blue, 650 nm, green and 700 nm, red (all within the R band). The scale of the panel (100 μm , or 2.96 arcsec) is shown next to the top left-hand panel. The CCD pixels have a size of 13.5 μm (0.4 arcsec) on the side.

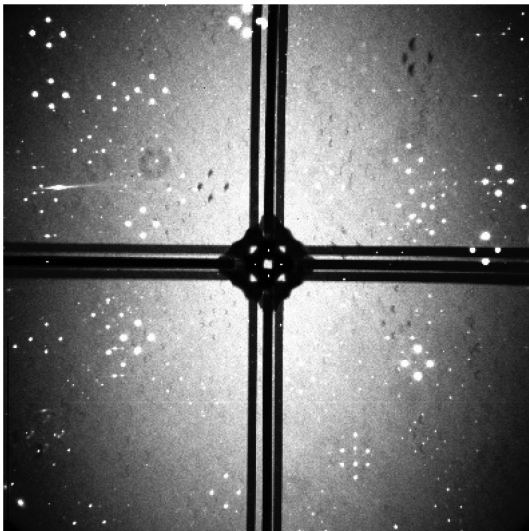


Figure 4. An exposure taken with RoboPol. The colors have been stretched to highlight features in the FOV. Background light in the central region is partially blocked using a focal-plane mask. The dark vertical and horizontal lines are the shadows cast by the mask supports. There is significant vignetting throughout the FOV, resulting in large-scale variations of the sky background intensity. Small-scale artefacts are also present and are due to the presence of dust specs at different locations within the instrument.

The design of the mask has to take care of two important considerations. First, reflection from the mask surface can impart erroneous polarization in the light from the astronomical source. Therefore, the mask surface was coated with a plastic material of 10–15 μm thickness on each surface to become non-reflective. Second, the size of the mask was selected to simultaneously (a) minimize photon contamination from the neighbourhood of the central target and (b) allow for enough area for background estimation around the target.

The inner portion of the mask (depicted in Fig. 5) measures 5.2 mm \times 5.2 mm \times 1 mm, and the full size including the supporting legs is 66.2 mm \times 66.2 mm \times 2.5 mm.

2.5 Control system and data-reduction pipeline

One of the design goals of the RoboPol instrument was to operate with high observation efficiency, which was achieved by fully automating the observing process. The RoboPol control system runs the telescope on robotic mode when the instrument is online, but allows the telescope to be run manually when the instrument is not in use. The control system features automated target acquisition, telescope focusing, dynamic exposure time calculation, and target of opportunity observations (including an alert system for GRBs).

The large amount of data generated by the survey is handled by an automated data-reduction pipeline, specifically developed for this purpose. The program performs aperture photometry of all point sources in the FOV, calculates their normalized Stokes parameters q and u , and also provides relative photometry. A detailed description of the RoboPol control system and pipeline is given in

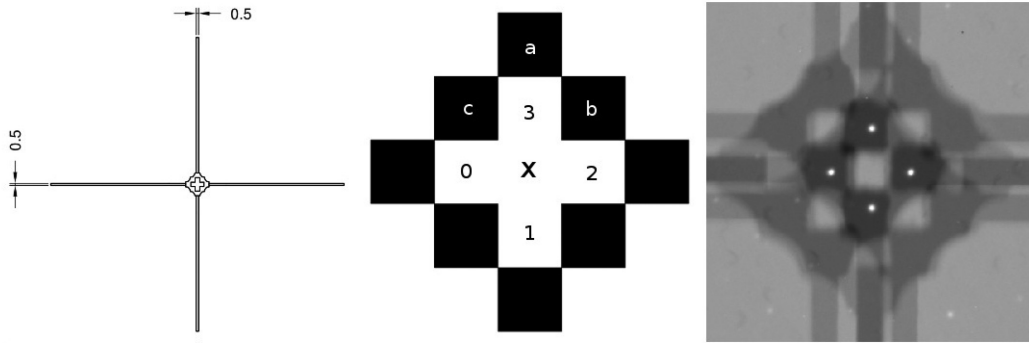


Figure 5. The RoboPol mask. Left: Design of mask and its supports, with the physical dimensions marked (in mm). Middle: Schematic of mask shape. White indicates open space, while dark indicates the presence of light-blocking material. Right: Zoom-in of a typical RoboPol science image showing a point source placed in the darkest shadows of the mask in the centre of the FOV. The linear shadows extending towards all edges of the image are cast by the supports of the mask.

King et al. (2014a). Upgrades made to the pipeline, mainly with regard to analysis in the wider FOV, are described in Panopoulou et al. (2015).

By default, the data are reduced and corrected for the instrumental polarization according to the instrument model described in King et al. (2014a) (see also Section 3). The parameters of the model are fit anew each observing season, as the instrument is removed from the GAM at the end of the observatory seasonal operations (typically November) and re-installed at the start of the following season (typically March). A separate model is constructed for each filter.

3 COMMISSIONING

The RoboPol instrument was designed, assembled, and tested at IUCAA before shipping to the Skinakas observatory for commissioning in 2013 May. The mechanical and optical elements of the design were found to be in excellent working order. Slight modifications were made to the telescope weight distribution. Well-known polarization standard stars were observed a multitude of times to validate the performance of both the instrument and the data-reduction pipeline.

During commissioning, a model of the instrumental response throughout the FOV was developed, as explained in King et al. (2014a). Unpolarized standard stars were used to raster map the FOV. These observations were then used to develop an instrument model; i.e. a set of functions that describe the variation of (a) the spot pattern, (b) the total intensity, and (c) the instrumental Stokes parameters across the FOV. The residuals resulting from subtraction of the model from the data are uniform across the field (see fig. 12 and also King et al. 2014a), testifying the effectiveness of the model to remove systematic large-scale patterns in the aforementioned parameters. The model is agnostic as to what optical effects it corrects for (e.g. vignetting, half-wave plate non-uniformity). All large-scale systematic effects expected to affect polarization measurement to the required accuracy are modeled out with this approach.

The on-sky characteristics of the PSF were compared to those predicted during the design phase. This comparison is made in terms of the fraction of total energy of a source that is enclosed within a circular aperture of given radius (curve of growth). We show a comparison between the curve of growth predicted from the Zemax model and those resulting from observations in Fig. 6. In

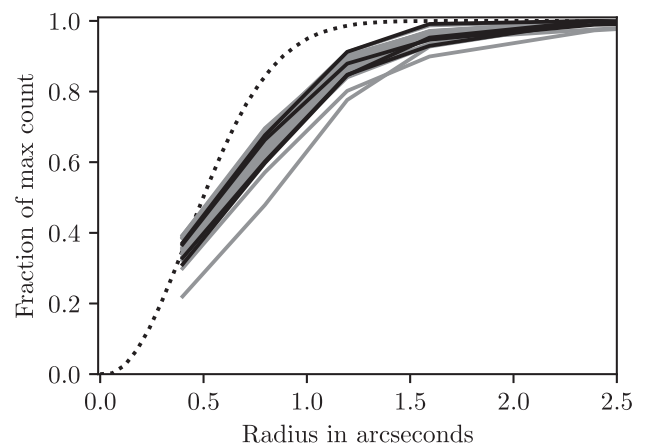


Figure 6. Fraction of total energy that is enclosed within an aperture of given radius (growth curve). The dotted line is the predicted curve from the Zemax software for a source at the center of the field (there is no significant difference between predictions for different spots of the same source). Solid grey lines show the observed growth curves for six sources located throughout the FOV (a separate curve is shown for each of the four spots), while the solid black lines are for a source in the centre of the field (within the mask).

order to minimize the effect of varying atmospheric seeing on this comparison, we have selected six sources observed during a night with median seeing $1''$. The exposure time was 20 s and the R -band magnitudes of the sources were in the range 12–16 mag. We show a separate curve of growth for each of the four spots of a source. We find significant differences between the observed and predicted curves. First, the observed curves of growth reach 90 per cent of the total light at a radius of 1.2–1.6 arcsec, which is 1.3–1.8 times larger than the radius expected from the Zemax model (0.9 arcsec). Second, the observed curves exhibit differences between the vertical and horizontal spots, something that is not found by the model. In particular, the two extreme curves that rise less steeply in Fig. 6 correspond to the horizontal spots of a source.

Such differences from the Zemax prediction are to be expected, as the prediction does not take into account a multitude of factors that are present in realistic situations (e.g. optical element misalignment, telescope tracking jitter, imperfect seeing conditions). In practice, we take care to perform photometry within apertures that enclose the majority of the energy of a source (e.g. Panopoulou et al. 2015), and

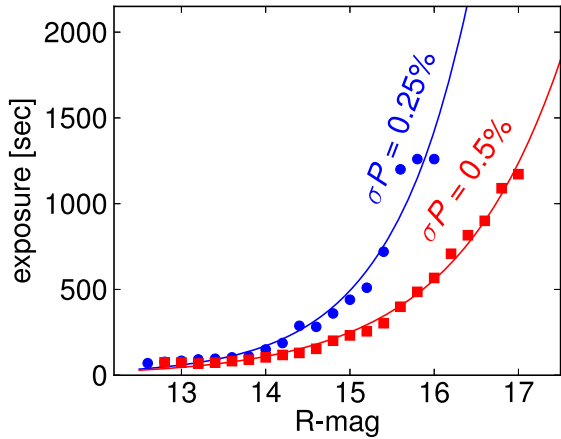


Figure 7. Required exposure time as a function of R -band magnitude in order to reach a σ_p of 0.25 per cent (blue) and 0.5 per cent (red). Squares and circles represent median values for multiple measurements obtained at different elevations, atmospheric conditions, and Moon phase. Curves show the exponential function fit to the data: $a e^{bx} + c$, with $(a, b, c) = (3.2 \times 10^{-5}, 1.09, 39)$ and $(0.0018, 0.79, -6)$ for a target σ_p of 0.25 per cent and 0.5 per cent, respectively.

demonstrate that this results in excellent instrument performance (see Section 4).

An addition made to the mechanical system was the introduction of a pump used to channel dry air on to the glass protecting the CCD to prevent water vapor condensation on its surface during nights with high humidity. Finally, a removable plastic cover was placed on the window of the instrument, during the time that the telescope was in the stow position, to prevent dust from settling on the surface of the first lens.

4 PERFORMANCE

In the 5 yr of RoboPol operations, the efficiency and accuracy of the instrument have surpassed design specifications. In terms of time efficiency, the combination of the instrument design (no moving parts) with the automated observing strategy have resulted in an average of 15 targets observed per night during the 3-yr monitoring programme.

We characterized the performance of the instrument in terms of exposure time using observing data of different sources placed within the mask throughout all observing seasons. The data used cover different elevations, atmospheric conditions, and Moon phases. In Fig. 7 we present the required exposure time in order to reach 0.25 per cent and 0.5 per cent (statistical) accuracy in polarization for sources of different magnitude.

4.1 R-band performance within the mask

4.1.1 Instrumental polarization

During the 5 yr of operation, standard calibrator stars were observed each night along with the science observations. These measurements allow us to evaluate the instrumental polarization and its uncertainty (systematic uncertainty) as a function of time. For our initial analysis we do not make use of the instrument model presented in Section 3. The literature values of standard stars used for calibration are shown in Table 2.

Table 2. Literature polarization of standard stars used for instrument calibration.

Name	$p(\%)$	$\chi(\circ)$	Band	Ref
BD+32 3739	0.025 ± 0.017	35.79°	V	1
G191B2B	0.061 ± 0.038	147.65°	V	1
HD 212311	0.034 ± 0.021	50.99°	V	1
HD 14069	0.022 ± 0.019	156.57°	V	1
BD+59 389	6.430 ± 0.022	$98.14^\circ \pm 0.10^\circ$	R	1
BD+33 2642	0.20 ± 0.15	$78^\circ \pm 20^\circ$	R	2
WD2149+021	0.05	-125°	R	3
HD 154892	0.05 ± 0.03	–	B	4
BD+40 2704	0.07 ± 0.02	$57^\circ \pm 9^\circ$?	5

Note: (1) Schmidt, Elston & Lupie (1992); (2) Skolidis et al. (2018); (3) Cikota et al. (2017); (4) Turnshek et al. (1990); and (5) Berdyugin & Teerikorpi (2002)

The instrument causes the observed Stokes parameters of standard stars, q_{obs} and u_{obs} , to be offset from their literature values, q^* , u^* , in a systematic way. In other words, the literature-corrected measurements $\bar{q} = q_{\text{obs}} - q^*$ and $\bar{u} = u_{\text{obs}} - u^*$ are found to be offset from (0,0) on the $\bar{q} - \bar{u}$ plane. Measurements of standard stars are shown on the $\bar{q} - \bar{u}$ plane in Fig. 8, grouped by year of observation. Each point is a single observation, with errors that are purely statistical (from photon noise). All observations have been processed by the RoboPol pipeline, *without* making use of the instrument model. This allows us to determine the systematic uncertainty due to the instrument alone, avoiding possible unknown errors due to modeling. The pipeline version used employs optimized aperture photometry as described in Panopoulou et al. (2015) with slight modifications presented in Skolidis et al. (2018).

For all years, the instrument introduces a fractional linear polarization at the level of $p_{\text{inst}} = 0.3 - 0.4$ per cent. This is found using the weighted mean of all \bar{q} and all \bar{u} measurements (black crosses in Fig. 8). The level of p_{inst} varies by less than 0.1 per cent throughout 5 yr of observing, during which there have been multiple removals and replacements of the instrument on the telescope.

The scatter of \bar{q} and \bar{u} measurements contains information on the level of random variation of the instrumental polarization. Normally this scatter is also influenced by a number of other factors: observational uncertainties in the measurements of the standard stars, atmospheric variations throughout the observing period, errors in the literature values of standards, and possible intrinsic variability of standards. Seeing has been found to significantly affect measurements of standard stars with a nearby source (within a few arcseconds). One example is Hiltner 960. This is because the second source is (partially or fully) blended with the calibrator star during nights with bad seeing. Słowikowska et al. (2016) find a similar problem with a source that lies 16 arcsec away from BD+59 389 using the RINGO3 polarimeter. We have found this not to be the case for our measurements, as the sources are well-separated for all the nights observed. Note that even though commonly used standard stars are assumed to be stable, we have found this not to be the case for a subset of regularly monitored stars. The wealth of data collected on standard stars throughout 5 yr of operation, along with the aforementioned stability of the instrument, has allowed us to identify a subset of standard stars that are variable. We have also found a number of stars that appear offset from the rest of the calibrators in the $\bar{q} - \bar{u}$ plane (and therefore have erroneous literature values). These stars are not included in this analysis, and we will dedicate a

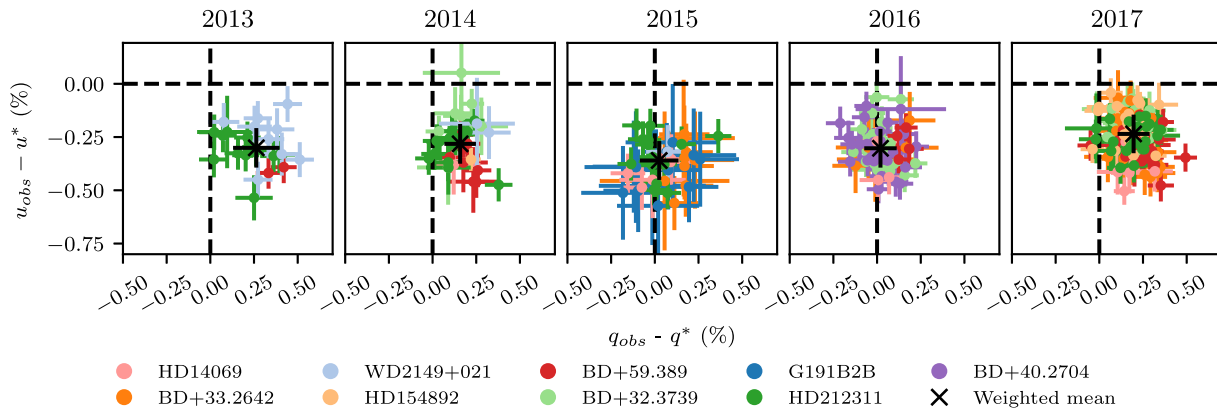


Figure 8. Standard star residuals from literature values (shown in Table 2) for all years of RoboPol operation. Each point is a single observation, processed without using the instrument model. A different colour is used for each star. Observations were conducted in the mask and in the R band. Error bars shown are only statistical. The black cross marks the weighted mean of all measurements. Dashed lines are for visualization of (0,0).

separate publication to present and discuss them (Blinov et al., in preparation).

In this analysis we only make use of standards that we trust have no or undetectable (below 0.1 per cent) intrinsic variability and have accurate literature values (these are the stars used for Fig. 8 as well). We investigate whether there are detectable variations of the polarization of standards within a season in Fig. 9, which shows the same observations as in Fig. 8 as a function of time. The lack of points in 2013 is due to the fact that very few high-quality standards were observed initially. As time progressed, we refined our set of observed standards. We also increased exposure times (resulting in reduced errors for the 2016, 2017 set) and frequency of observations within a given night.

In order to de-couple these effects from the instrumental polarization variability, we adopt a novel approach. First, we make use only of the aforementioned well-behaved standards. We then make the assumption that the instrumental variability in q and in u follows Gaussian distributions and we treat q and u independently. The errors on the measured \bar{q} , \bar{u} are Gaussian (photon signal-to-noise ratios are of order 10^3). In this case, the likelihood function for the instrument variability can be found analytically, and is given by equation A5 in Venters & Pavlidou (2007).

We calculate the normalized likelihoods for the systematic uncertainty of the instrumentally induced normalized Stokes parameters q_{inst} and u_{inst} separately, using measurements obtained in a single observing year with RoboPol (Fig. 10). The maximum likelihood scatter of the instrument polarization is found to be $\sigma_{\text{inst}} = 0.051 - 0.054$ per cent for both q and u . Values within this range are found when using the observations of 2016 (74 measurements) and of 2017 (130 measurements). However, for smaller numbers of observations the error in the maximum likelihood estimate will be larger. This is the case for the years 2013, 2014, and 2015, where only 23, 33, and 47 measurements can be used for the determination of the instrumental polarization. In these initial seasons, many standards were observed that were in fact variable. Some of these stars were used for the initial determination of the instrument performance (King et al. 2014a).

It may also be argued that part of the systematic variability measured could arise from the fact that we are using observations throughout an entire season (May–November) for its determination. This is not the case, however, as we do not find a significant shift in the \bar{q} or \bar{u} measurements at different dates within a season, as evidenced by inspection of Fig. 9.

We now explore how the introduction of the instrument model may change the above conclusions. To this end, we processed the 2017 set of standards using the model built in the same year (using the star HD 212311). As expected, we find the residuals to be reduced: the weighted mean \bar{q} is -0.07 per cent and that of \bar{u} is 0.017 per cent (compared to 0.18 and -0.24 per cent without the model correction). We find that the maximum likelihood scatter in the instrument polarization in 2017, after applying the model is $\sigma_{\text{inst},q} = 0.054$ per cent, $\sigma_{\text{inst},u} = 0.052$ per cent, consistent with that found without using the model correction (0.051 per cent and 0.053 per cent, respectively).

4.1.2 Instrumental rotation

Aside from the offset on the $\bar{q} - \bar{u}$ plane, another instrumental effect is a rotation of the instrument frame compared to the celestial frame. We can measure this rotation by using polarized standard stars, which have known and well-measured polarization angles (χ^*). In order to measure the rotation, we first correct each measurement of a polarized standard for the instrumental zero-point offset found previously. In practice, we subtract q_{inst} and u_{inst} from each measurement of the polarized standard and propagate the errors. Then, we find the (corrected for zero-point-offset) polarization angle $\chi_{\text{obs},c}$ and subtract from it the literature value χ^* . Any deviation from 0 points to an instrument frame rotation (compared to the sky).

These differences are shown in Fig. 11, for all years of RoboPol operation.⁶ There is considerable scatter not only between observations of different stars but also between the measurements of an individual star compared to the errors. This is most likely a result of the variable nature of the majority of these standards (HD183143, HD204827, Bastien et al. 1988; HD155197, HD236633, Hiltner960, Schmidt et al. 1992; HD150193, Hubrig et al. 2011). Their variability excludes them from being used to measure the zero-point offset. However, because they are highly polarized, they can still serve for estimating the instrumental polarization angle rotation. Another source that could be contributing to the observed scatter is

⁶Literature values for the polarized standard stars in Fig. 11 were taken from Schmidt et al. (1992) for BD+59.389, BD+64.104, HD 155197, HD 236633, Hiltner 960; from Whittet et al. (1992) for HD 150193, HD 215806; and from Hsu & Breger (1982) for HD 183143, HD 204827.

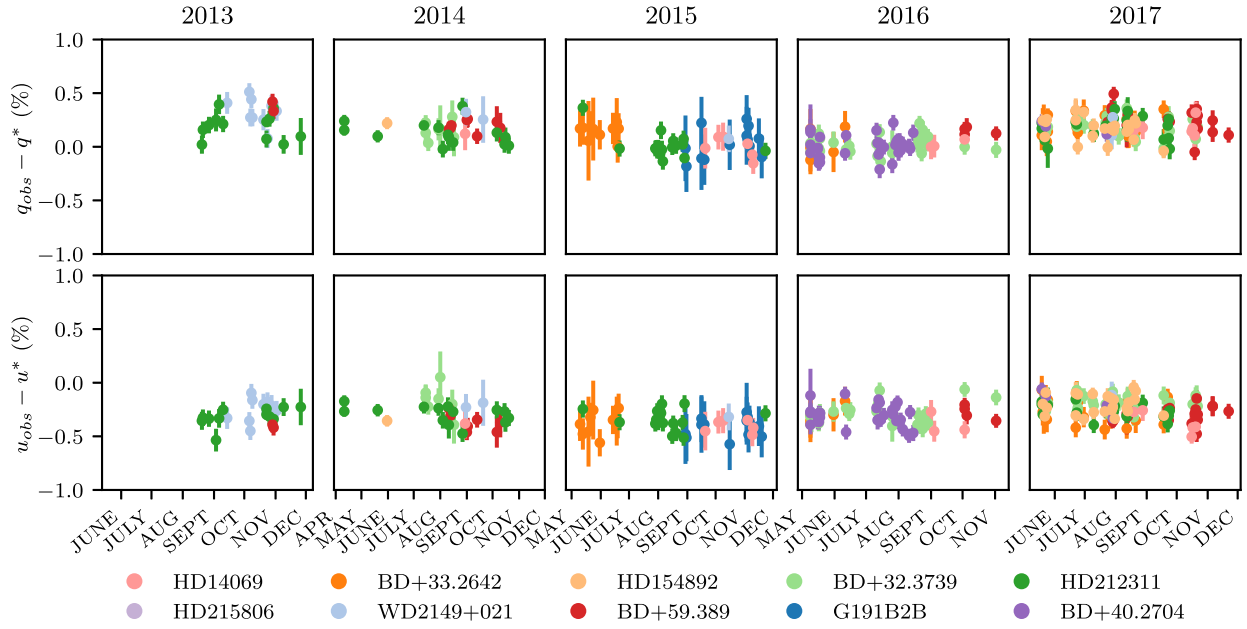


Figure 9. The same measurements of Fig. 8 but shown as a function of observing date for all years of RoboPol operation.

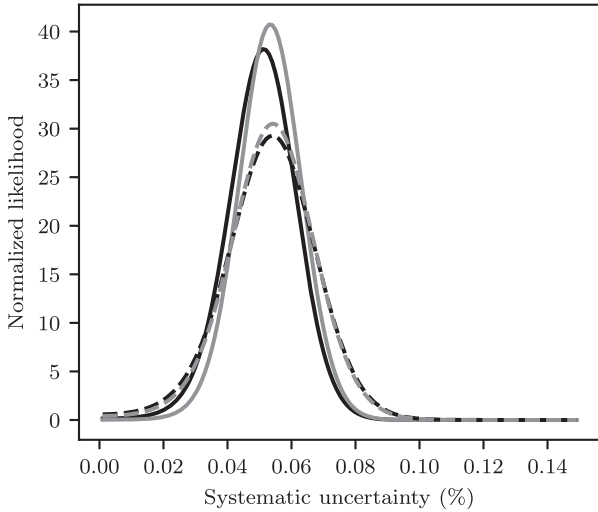


Figure 10. The normalized likelihoods for the systematic uncertainty of q_{inst} (black) and u_{inst} (grey) in the mask, calculated using measurements of standard stars (Fig. 8) from 2016 (dashed) and 2017 (solid). The maximum-likelihood systematic uncertainty is $\sigma_{\text{inst}} = 0.051\text{--}0.054$ per cent.

the variation of the instrument coordinate system that results from removal and repositioning of the instrument on the telescope (which happens up to 2–3 times throughout an observing season). With the existing data set, we cannot distinguish between these two sources of uncertainty. However, even with the uncertainties introduced, we find the weighted mean instrumental polarization angle rotation (solid blue line) to be $0.5^\circ < \chi_{\text{inst}} < 1.2^\circ$ for all years.

For the year 2013, the instrument rotation found here is smaller than that found in King et al. (2014a) ($2.31^\circ \pm 0.34^\circ$). This difference arises mainly from the fact that we do not make use of the standard star VI Cyg #12 (Schmidt et al. 1992) in our analysis (which shows signs of strong variability in our data), and include the star HD 183143. If we use the same sample as King et al.

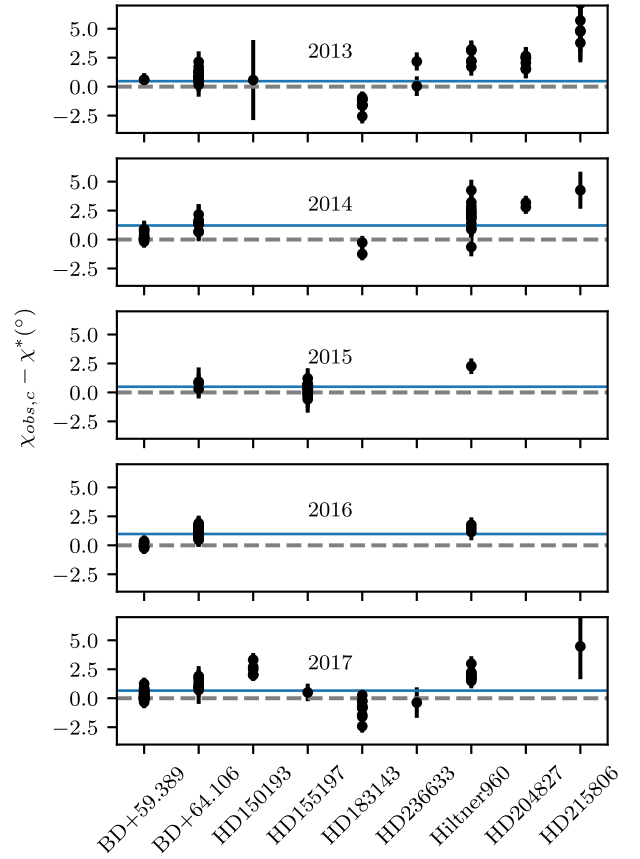


Figure 11. Rotation of the instrument reference frame compared to the celestial frame measured with polarized standard stars. All years from 2013 (top) to 2017 (bottom). The dashed line marks a rotation of 0° . The mean rotation for each year is marked by the solid blue line.

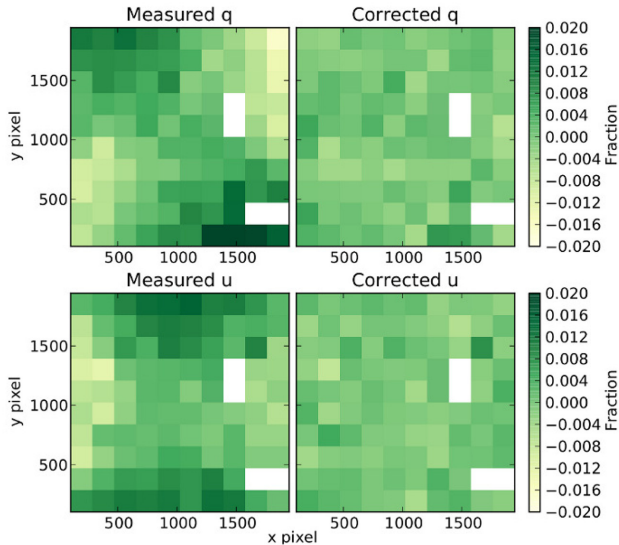


Figure 12. Comparison between q and u measurements of an unpolarized standard star positioned throughout the field: left, without model correction, and right, with model correction. White squares are due to the absence of measurements in those positions.

(2014a), we find values consistent within 1σ . This underscores the necessity of establishing a large set of reliable polarized standards, to allow a precise determination of the instrument reference frame rotation.

4.2 R-band performance throughout the FOV

As discussed in Section 2 the instrumental response is a function of target position on the FOV. To characterize this response for the entire FOV, we make use of the instrument model. As demonstrated in King et al. (2014a), the instrument model is capable of removing the large-scale patterns seen in the instrumental q and u . Fig. 12 shows R -band q and u measurements of the unpolarized standard star HD 212311, which was used to create the model of 2017. The instrumental polarization prior to model correction is shown in the left-hand panels (top for q , bottom for u). The residuals after model correction (shown in the right-hand panels) are spatially uniform and lie below a level of 0.3 per cent. The systematic uncertainty outside the mask remains at these levels for models taken in different years of RoboPol operation (compare with King et al. 2014a; Panopoulou et al. 2015).

Apart from the large-scale spatial variations in the instrument response, there exist small-scale features that affect the instrumental polarization locally. These small-scale features are due to the presence of dust particles that lie within the instrument. The particles cast shadows in different positions in the FOV, as can be seen in Fig. 4. Due to the design of RoboPol, these features cannot be simply corrected for by flat-fielding. Our approach is to detect these features in flat-field images (taken with the telescope pointed at the sky during twilight), and then discard any targets that happened to be observed on the position of a dust spec. This procedure is explained in detail by Panopoulou et al. (2015).

4.3 Instrument characterization in B , V , and I bands

The majority of observations are performed in the R band. However, some of the other RoboPol projects require multiwave-

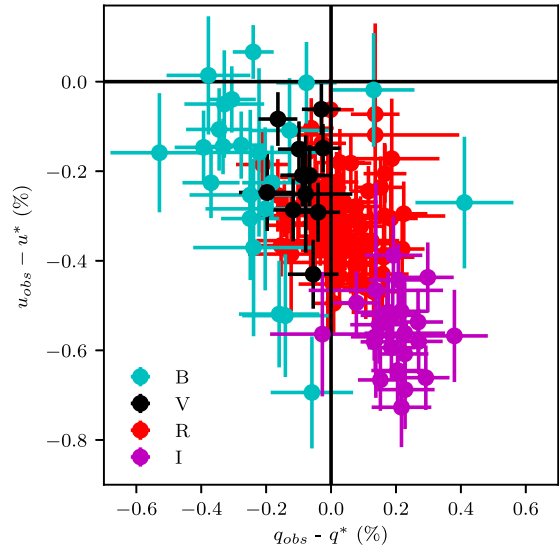


Figure 13. Comparison between q and u residuals of standard stars in the mask (from their literature values) observed during 2016 in the B , V , R , and I bands. The measurements have not been corrected for instrumental polarization (using the model).

length measurements. Due to the relative scarcity of standard star observations compared to the R band, we cannot perform a similarly rigorous characterization of the instrument in the B , V , and I bands. For this reason, we consider data from the year 2016 within which the most observations of standard stars in these bands were taken. Fig. 13 shows q and u measurements of standards observed in the B , V , R , and I bands in the mask. No model correction has been applied to the data. We find that the mean instrumental polarization in the mask varies within 0.6 per cent between bands. The weighted mean p_{inst} in the different bands are 0.29 ± 0.16 per cent (B), 0.21 ± 0.099 per cent (V), 0.30 ± 0.091 per cent (R), 0.6 ± 0.077 per cent (I), where the quoted uncertainty was calculated from the standard deviation of \bar{q} , \bar{u} measurements.

For each band, a separate model is created in each observing year. We explore the effectiveness of the model in Fig. 14. The panels (B , V , I from top to bottom) show the residuals after model correction for 2017. The residuals are spatially uniform, as is the case for the R -band model. In all three bands the rms residuals are at the same level as in the R band. There are a number of positions that are empty, as a result of poor sampling of the FOV during production of the raster map. This would only affect the analysis of targets outside the mask (falling in the regions with gaps). However, all multiband observations have placed targets in the mask, where the instrumental polarization is best understood. The presented models have been adequate for the purpose of removing of instrumental polarization in the mask.

Several artificial effects appear in the B and I bands, which render the task of controlling systematics outside the mask more difficult than in the R band.

One artefact that occurs in the B band is the appearance of ghost images near relatively bright stars. An example of such images is shown in Fig. 15 (top) for a source placed in the mask (left) and for a pair of sources in the field (right). The exposure time was 5 s and the central source has an R magnitude of ~ 9 . In the case of the source in the mask, the background sky is too faint for the shadow of the mask to be clearly visible (as a result of the short exposure

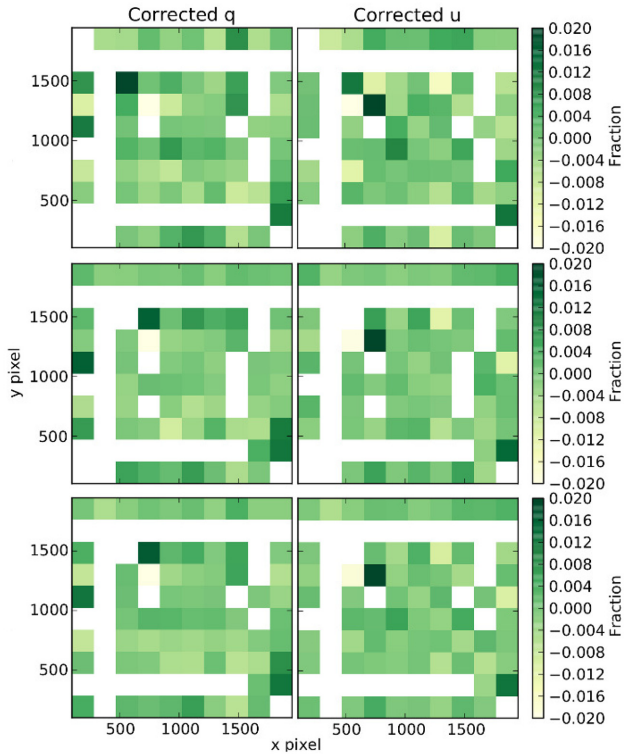


Figure 14. Residuals instrumental q (left) and u (right) after model correction throughout the FOV. From top to bottom: B , V , and I bands.

time). The pattern of the ghosts is similar in both cases, but the ghost images are brighter for the source in the mask (these brighter ghosts are marked with yellow lines in the figure). This artefact appears to be the result of increased reflectivity of the antireflection coating on the CCD window.

A second effect in the B band is the appearance of a periodic striped pattern that runs diagonally throughout the FOV. This is best seen in the flat-field image of Fig. 15 (middle). The intensity variations caused by this pattern are of order 1 per cent. This effect is also seen in images taken with the same camera, but without RoboPol, and hence is not related to the instrument.

A final artefact is seen in the I band, where a pattern of fringes appears in the background far from the center of the field. These I -band fringes are quite typical of thinned back illuminated CCDs (e.g. Howell 2012). They are caused by thin film interference effects for light of longer wavelengths, between the various CCD layers that result in quantum efficiency variations in CCD pixels. An example sub-field of the FOV that exhibits fringing is shown in Fig. 15 (bottom). The reduction in brightness within the fringes is 1–2 per cent.

5 SUMMARY

We have presented the RoboPol four-channel imaging polarimeter, developed for use at the Skinakas observatory 1.3 m telescope in Crete, Greece. It has been operating since it was commissioned in 2013. The main task of RoboPol has been to monitor the linear polarization of a large sample of blazars in the R -band from 2013 to 2015, as part of the RoboPol programme. RoboPol has delivered science for a number of other projects, including Be/X-ray binary and interstellar medium studies.

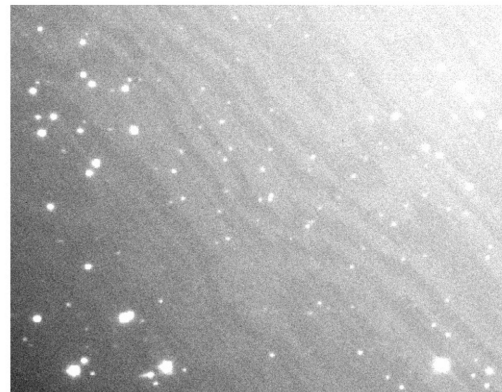
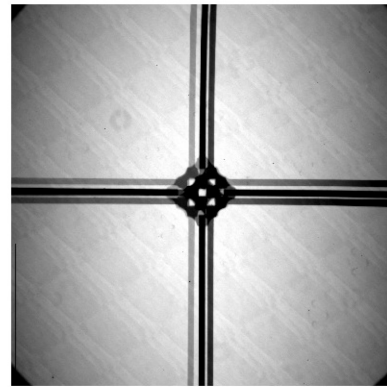
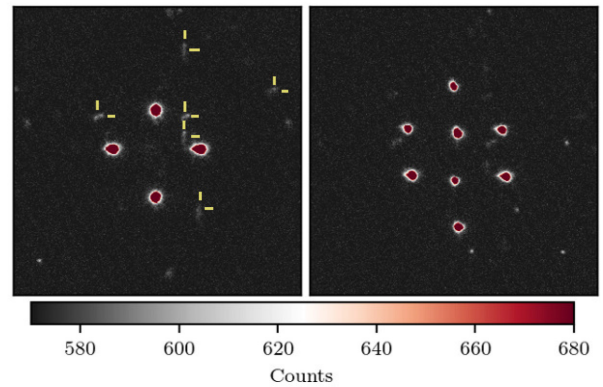


Figure 15. Artefacts in the B and I bands. Top: B -band ghosts around bright stars. Left: a source in the mask. Each ghost is marked with a vertical and horizontal yellow line. Right: a pair of sources in the field. Middle: Sky flat-field taken in the B band. The colors have been stretched to highlight the periodic patterns seen throughout the FOV. Bottom: Zoom in to a region of the FOV where fringes are visible in the I band (exposure time was 2 min).

The design of RoboPol makes use of two WPs and two non-rotating half-wave plates to produce simultaneous measurements of the Stokes q and u parameters.

The R -band performance of RoboPol is stable throughout an observing season and varies very little during 5 yr of regular operation. The scatter in the offset (or instrumental polarization) for R -band measurements in the central mask region is below 0.1 per cent (0.05 per cent maximum likelihood value) in fractional linear polarization. Measurements can be performed for point sources throughout the 13.6×13.6 arcmin FOV in the R band where systematic offsets are controlled at the level of 0.3 per cent.

ACKNOWLEDGEMENTS

We thank Anna Steiakaki for her invaluable contribution and technical support; John Kypriotakis for helping with edits in the paper; and the anonymous reviewer for their suggestions.

The RoboPol project is a collaboration between Caltech in the USA, MPIfR in Germany, Toruń Centre for Astronomy in Poland, the University of Crete/FORTH in Greece, and IUCAA in India. The U. of Crete group acknowledges support by the ‘RoboPol’ project, which is implemented under the ‘Aristeia’ Action of the ‘Operational Programme Education and Lifelong Learning’ and is co-funded by the European Social Fund (ESF) and Greek National Resources, and by the European Commission Seventh Framework Programme (FP7) through grants PCIG10-GA-2011-304001 ‘Jet-Pop’, and PIRSES-GA-2012-31578 ‘EuroCal’. This research was supported in part by NASA grant NNX11A043G and NSF grant AST-1109911, and by the Polish National Science Centre, grant numbers 2011/01/B/ST9/04618 and 2017/25/B/ST9/02805. K. T. and G. P. acknowledge support by the European Commission Seventh Framework Programme (FP7) through the Marie Curie Career Integration Grant PCIG-GA-2011-293531 ‘SFOnset’. A.N.R., G.P., and A.C.S.R. acknowledge support from the National Science Foundation, under grant number AST-1611547. K. T. and D. B. acknowledge support from the European Research Council under the European Union’s Horizon 2020 research and innovation programme, grant agreement No. 771282. M. B. acknowledges support from the International Fulbright Science and Technology Award. I.M. was funded by the International Max Planck Research School (IMPRS) for Astronomy and Astrophysics at the Universities of Bonn and Cologne. T. H. was supported by the Academy of Finland project number 317383. This research made use of Astropy, <http://www.astropy.org>, a community-developed core PYTHON package for Astronomy.

REFERENCES

- Abdo A. A. et al., 2010, *Nature*, 463, 919
 Afanasiev V. L., Amirkhanyan V. R., 2012, *Astrophys. Bull.*, 67, 438
 Angelakis E. et al., 2016, *MNRAS*, 463, 3365
 Appenzeller I., 1967, *PASP*, 79, 136
 Bastien P., Drissen L., Menard F., Moffat A. F. J., Robert C., St-Louis N., 1988, *AJ*, 95, 900
 Berdyugin A., Teerikorpi P., 2002, *A&A*, 384, 1050
 Bjornsson C.-I., 1982, *ApJ*, 260, 855
 Blinov D. et al., 2015, *MNRAS*, 453, 1669
 Blinov D. et al., 2016a, *MNRAS*, 457, 2252
 Blinov D. et al., 2016b, *MNRAS*, 462, 1775
 Blinov D. et al., 2018, *MNRAS*, 474, 1296
 Cikota A., Patat F., Cikota S., Faran T., 2017, *MNRAS*, 464, 4146
 Covino S. et al., 2014, *Astron. Nachr.*, 335, 117
 Devogèle M. et al., 2017, *MNRAS*, 465, 4335
 Fujita K., Itoh Y., Mukai T., 2009, *Adv. Space Res.*, 43, 325
 Geyer E. H., Jockers K., Kiselev N. N., Chernova G. P., 1996, *Ap&SS*, 239, 259
 Helhel S., Khamitov I., Kahya G., Bayar C., Kaynar S., Gumerov R., 2015, *Exp. Astron.*, 39, 595
 Hough J. H., Lucas P. W., Bailey J. A., Tamura M., Hirst E., Harrison D., Bartholomew-Biggs M., 2006, *PASP*, 118, 1302
 Hovatta T. et al., 2016, *A&A*, 596, A78
 Howell S. B., 2012, *PASP*, 124, 263
 Hsu J.-C., Breger M., 1982, *ApJ*, 262, 732
 Hubrig S. et al., 2011, *A&A*, 536, A45
 Kawabata K. S. et al., 2008, in *Ground-based and Airborne Instrumentation for Astronomy II*. Bellingham, WA. p. 70144L
 Kiehlmann S., Blinov D., Pearson T. J., Liodakis I., 2017, *MNRAS*, 472, 3589
 Kikuchi S., Inoue M., Mikami Y., Tabara H., Kato T., 1988, *A&A*, 190, L8
 King O. G. et al., 2014a, *MNRAS*, 442, 1706
 King O. G. et al., 2014b, *MNRAS*, 445, L114
 Konigl A., Choudhuri A. R., 1985, *ApJ*, 289, 188
 Laher R. R., Gorjian V., Rebull L. M., Masci F. J., Fowler J. W., Helou G., Kulkarni S. R., Law N. M., 2012, *PASP*, 124, 737
 Liodakis I., Blinov D., Papadakis I., Pavlidou V., 2017, *MNRAS*, 465, 4783
 Magalhaes A. M., Rodrigues C. V., Margoniner V. E., Pereyra A., Heathcote S., 1996, in *Roberge W. G., Whittet D. C. B., eds, ASP Conf. Ser. Vol. 97, Polarimetry of the Interstellar Medium*. Astron. Soc. Pac., San Francisco, p. 118
 Oliva E., 1997, *A&AS*, 123, 589
 Panopoulou G. et al., 2015, *MNRAS*, 452, 715
 Panopoulou G. V., Psaradaki I., Tassis K., 2016, *MNRAS*, 462, 1517
 Pavlidou V. et al., 2014, *MNRAS*, 442, 1693
 Pernechele C., Giro E., Fantinel D., 2003, in *Fineschi S., ed., Proc. SPIE Vol. 4843, Polarimetry in Astronomy*. SPIE, Bellingham, p. 156
 Pirola V., Berdyugin A., Berdyugina S., 2014, in *Ground-based and Airborne Instrumentation for Astronomy V*. Bellingham, WA, p. 91478I
 Raiteri C. M. et al., 2017, *MNRAS*, 466, 3762
 Ramaprakash A. N., Gupta R., Sen A. K., Tandon S. N., 1998, *A&AS*, 128, 369
 Reig P., Blinov D., 2018, *A&A*, 619, A19
 Reig P., Blinov D., Papadakis I., Kylafis N., Tassis K., 2014, *MNRAS*, 445, 4235
 Reig P., Blay P., Blinov D., 2017, *A&A*, 598, A16
 Scarrott S. M., Warren-Smith R. F., Pallister W. S., Axon D. J., Bingham R. G., 1983, *MNRAS*, 204, 1163
 Schmidt G. D., Elston R., Lupie O. L., 1992, *AJ*, 104, 1563
 Sillanpää A., Takalo L. O., Nilsson K., Kikuchi S., 1993, *Ap&SS*, 206, 55
 Skalidis R., Panopoulou G. V., Tassis K., Pavlidou V., Blinov D., Komis I., Liodakis I., 2018, *A&A*, 616, A52
 Słowikowska A., Krzeszowski K., errorZdotejmo M., Reig P., Steele I., 2016, *MNRAS*, 458, 759
 Słowikowska A., Krzeszowski K., errorZdotejmo M., Blinov D., Reig P., 2018, *MNRAS*, 479, 5312
 Turnshek D. A., Bohlin R. C., Williamson R. L., II, Lupie O. L., Koornneef J., Morgan D. H., 1990, *AJ*, 99, 1243
 Uemura M. et al., 2017, *PASJ*, 69, 96
 Venters T. M., Pavlidou V., 2007, *ApJ*, 666, 128
 Whittet D. C. B., Martin P. G., Hough J. H., Rouse M. F., Bailey J. A., Axon D. J., 1992, *ApJ*, 386, 562
 Wiktorowicz S. J., Nofi L. A., 2015, *ApJ*, 800, L1
 Żejmo M., Słowikowska A., Krzeszowski K., Reig P., Blinov D., 2017, *MNRAS*, 464, 1294

This paper has been typeset from a $\text{\TeX}/\text{\LaTeX}$ file prepared by the author.